

Hierarchical mesoporous S,N-codoped carbon nanostructures composed of Co/Co-Cu-S/carbon nanoplate arrays on carbon nanofibers as a self-supported air cathode for long-lasting rechargeable Zn-air batteries

XU ZhuYing^{1†}, YAN Lei^{1†}, SHEN JunLing¹, YANG XiaoJing¹, NING JiQiang²,
ZHONG YiJun¹ & HU Yong^{1,3*}

¹ Key Laboratory of the Ministry of Education for Advanced Catalysis Materials, Department of Chemistry, Zhejiang Normal University, Jinhua 321004, China;

² Department of Optical Science and Engineering, Fudan University, Shanghai 200438, China;

³ Hangzhou Institute of Advanced Studies, Zhejiang Normal University, Hangzhou 311231, China

Received July 30, 2021; accepted October 11, 2021; published online December 31, 2021

One of the primary roadblocks to widespread applications of rechargeable Zn-air batteries is the durability issue with oxygen reduction and evolution processes (ORR/OER) bifunctional electrocatalysts. We herein report the construction of a self-supported air cathode for Zn-air batteries made of S,N-codoped porous complex carbon nanostructures of Co/Co-Cu-S/carbon nanoplate arrays and carbon nanofibers (denoted as Co/Co-Cu-S@SNPCP-CFs). The hierarchical heteroatom-doped mesoporous carbon nanohybrids with multiple active species not only provide a high surface-to-volume ratio, exposing more catalytic sites and accelerating the charge and mass transfer, but also boost the activity and durability. The Co/Co-Cu-S@SNPCP-CFs catalyst reveals a small potential gap ($\Delta E=0.67$ V) between the half-wave potential of ORR and OER potential at 10 mA cm^{-2} , demonstrating outstanding bifunctional performance. Furthermore, the rechargeable Zn-air battery made with the as-obtained electrocatalyst exhibits a high-power density of 220 mW cm^{-2} and a long cycling time of over 800 h at 10 mA cm^{-2} , and the flexible solid-state rechargeable Zn-air battery based on Co/Co-Cu-S@SNPCP-CFs self-supporting air cathode also displays a long duration time of over 60 h.

Co, Co-Cu-S, carbon, bifunctional electrocatalyst, rechargeable Zn-air batteries

Citation: Xu Z Y, Yan L, Shen J L, et al. Hierarchical mesoporous S,N-codoped carbon nanostructures composed of Co/Co-Cu-S/carbon nanoplate arrays on carbon nanofibers as a self-supported air cathode for long-lasting rechargeable Zn-air batteries. *Sci China Tech Sci*, 2022, 65: 693–703, <https://doi.org/10.1007/s11431-021-1942-6>

1 Introduction

Rechargeable Zn-air batteries have been considered one of the most promising energy storage systems for their high theoretical energy density of 1086 Wh kg^{-1} , availability of

abundant raw materials, as well as high safety and low cost [1–3]. In particular, they have been developed as flexible power sources for wearable electronics, microcomputers, and smartphones in recent years [4,5]. However, the practical application of rechargeable Zn-air batteries encounters the bottlenecks of a short lifetime, mainly originating from the slow kinetics of oxygen reduction reaction (ORR) and oxygen evolution reaction (OER) at cathode electrodes [6,7].

[†]These authors contributed equally to this work.

*Corresponding author (email: yonghu@zjnu.edu.cn)

Meanwhile, the inactive and polymeric binders as the “dead mass” in the manufacture of catalytic electrodes further exacerbate the lifetime problem [8,9]. Till now, air cathodes derived from precious metals, such as platinum (Pt) and ruthenium (Ru), have been systematically studied, which are considered to be state-of-the-art electrocatalysts with high ORR or OER activities. However, limitations of high-cost, insufficient bifunctionality, and unsatisfactory stability hinder their commercial applications [10,11]. Therefore, it is of significance to develop cost-effective self-supporting electrodes for rechargeable Zn-air batteries which hold high-activity and long-lasting bifunctional active sites.

To date, much research effort has been devoted to developing efficient bifunctional oxygen electrocatalysts by integrating multiple active components [12,13]. It has been found that hybrid materials consisted of transition metal chalcogenides and heteroatom-doped (such as N, S, P) carbon substrates exhibit excellent ORR and/or OER activities [14,15]. Among them, transition metal sulfides possess a high conductivity and intrinsic activity to facilitate the OER process [16]. Meanwhile, inserting heteroatoms in carbon materials boosts the delocalization of asymmetrical charges for positively charging the adjacent carbon atoms, which creates more highly effective active sites and promotes the ORR process [17,18]. Thus, constructing hybrid electrocatalysts from transition metal sulfides and carbon substrates brings many intrinsic advantages, such as multiple active sites, high electrical conductivities, and long-lifetime stabilities, for practical applications [19–21]. The air electrode of Zn-air batteries involves three-phase interface reaction and a precise design of electrode structures is crucial for achieving a high power-output and cycle-stability [22–24]. Specifically, fabricating porous hybrid nanostructures effectively alleviates the issue of volume change during charging and discharging processes to improve cycle stability [25]. Therefore, strategies of integrating active catalytic species with well-defined porous carbon substrates are highly desired to obtain self-supported air electrodes, which endows Zn-air batteries with a high-efficiency and long-cycle-life.

Motivated by this, we herein have designed and fabricated a bifunctional oxygen electrocatalyst as a self-supporting air electrode for long-lasting Zn-air batteries. The electrode is fabricated through combining S,N-codoped mesoporous carbon nanostructures of Co/Co-Cu-S/carbon nanoplates and carbon nanofibers (denoted as Co/Co-Cu-S@SNPCP-CFs). In this design, CdS nanoparticles (NPs) as pore formers and sulfur sources endow the resultant electrocatalysts with multiple merits: (1) the pore formation increases specific surface areas and pore volumes for facilitating mass transport and exposes more catalytic sites; (2) metal sulfides and S-doped porous carbon frameworks promote OER and ORR kinetics; and (3) the synergistic coupling between active metal-based sites and three-dimensional (3D) porous het-

eroatoms-doped carbon hybrid structures improves the stability of electrocatalysts. The resultant catalyst of Co/Co-Cu-S@SNPCP-CFs exhibits a superior bifunctional catalytic activity and robust stability for ORR and OER with a reversible oxygen overpotential of 0.67 V. The rechargeable Zn-air battery using the Co/Co-Cu-S@SNPCP-CFs catalyst as the air electrode demonstrates a high-power density of 220 mW cm^{-2} and superior cycle stability of over 800 h at 10 mA cm^{-2} . Furthermore, the Co/Co-Cu-S@SNPCP-CFs based freestanding flexible solid-state rechargeable Zn-air battery delivers robust flexibility, high discharge power density, and excellent cycle stability ($> 60 \text{ h}$), indicating promising potentials for practical applications.

2 Experimental

2.1 Synthesis procedures

2.1.1 Synthesis of CdS NPs

In a typical synthesis, 1.08 g of $\text{Cd}(\text{NO}_3)_2 \cdot 4\text{H}_2\text{O}$, 0.27 g of thiourea, and 0.39 g of polyvinyl pyrrolidone (PVP) (K30) were added to 35 mL of ethylene glycol by stirring for 1 h. Then, the mixture solution was transferred into a 45 mL of polytetrafluoroethylene (PTFE)-lined stainless-steel autoclave and maintained at 140°C for 4 h. After natural cooling, the bright yellow CdS NPs were collected by centrifugation and washed with distilled water, then dried at 80°C overnight under vacuum.

2.1.2 Synthesis of CdS@PAN nanofibers

0.5 g of polyacrylonitrile (PAN) ($M_w=150000$) and 100 mg of CdS NPs were dispersed in 5 mL of *N,N*-dimethylformamide (DMF) by stirring for at least 8 h. Then, the mixture solution was loaded into a 5 mL syringe with a 20-gauge tip needle. The high voltage, feeding rate, and distance between the cathode and the anode were fixed at 13 kV, 0.05 mm min^{-1} and 15 cm, respectively, for the electrospinning.

2.1.3 Synthesis of CdS@PAN@CoCu-ZIF nanofibers

0.582 g of $\text{Co}(\text{NO}_3)_2 \cdot 6\text{H}_2\text{O}$ and 0.097 g of $\text{Cu}(\text{NO}_3)_2 \cdot 3\text{H}_2\text{O}$ were dissolved in 40 mL of distilled water with the molar ratios of $\text{Co}^{2+}/\text{Cu}^{2+}=5:1$. Then, the above mixture was quickly poured into 40 mL of distilled water containing 1.32 g of 2-methylimidazole (2-MIM). After being stirred for 1 min, 250 mg of CdS@PAN nanofibers was immersed into the formed purple solution and aged for 2 h at room temperature. The CdS@PAN@CoCu-ZIF nanofibers were harvested after being rinsed with ethanol several times and dried at 60°C for 3 h in a vacuum oven.

2.1.4 Synthesis of Co/Co-Cu-S@SNPCP-CFs

The obtained CdS@PAN@CoCu-ZIF nanofibers were

placed into a porcelain boat and calcined at 800°C with a heating rate of 2°C min⁻¹ under N₂ atmosphere for 2 h to obtain the final product.

2.1.5 Synthesis of Co/CoS₂@SNPCP-CFs, CuS@SNPCP-CFs, and Co/Cu@NPCP-CFs

The control samples of Co/CoS₂@SNPCP-CFs, CuS@SNPCP-CFs, and Co/Cu@NPCP-CFs catalysts were synthesized similarly to the process of Co/Co-Cu-S@SNPCP-CFs, but without adding Cu(NO₃)₂·3H₂O, Co(NO₃)₂·6H₂O, and CdS NPs, respectively.

2.2 Materials characterizations

X-ray diffraction (XRD) analyses of samples were obtained by on a Bruker D8 Advance diffractometer with Cu K α radiation. Scanning electron microscopy (SEM) images were performed on Hitachi S-4800 scanning electron micro-analyzer with an acceleration voltage of 15 kV. Transmission electron microscopy (TEM) and high-resolution TEM (HRTEM) and elemental mappings were carried out on a JEM-2100F field emission TEM at 200 kV. X-ray photoelectron spectroscopy (XPS) was determined on an ESCA-Lab MKII X-ray photoelectron spectrometer with Mg K α X-ray as the excitation source. Nitrogen adsorption-desorption isotherms were obtained at 77 K with Micrometrics ASAP 2020. Raman spectra were recorded on a Renishaw in Via-Refls with 532 nm laser excitation.

The detailed process of electrochemical measurements and the assembly procedure of Zn-air batteries are supplied in the Supporting Information.

3 Results and discussion

The synthetic scheme of the Co/Co-Cu-S@SNPCP-CFs catalyst is illustrated in Figure 1. First, CdS NPs with an

average diameter about 100 nm were prepared by a facile solvothermal method (Figure S1). Afterward, CdS@PAN nanofibers were obtained by an electrospinning technique: CdS NPs and PAN are dispersed in DMF as the working liquid for electrospinning (Figure S2). Subsequently, uniform triangle plates of Co,Cu-zeolitic imidazolate framework (CoCu-ZIF) grew on the surfaces of CdS@PAN nanofibers by introducing Co(NO₃)₂·6H₂O, Cu(NO₃)₂·3H₂O, and 2-MIM at room temperature (Figure S3). After a pyrolysis process under a N₂ atmosphere, the CdS@PAN@CoCu-ZIF nanofibers were converted into Co/Co-Cu-S@SNPCP-CFs. During the pyrolysis process, the organic ligand in the CoCu-ZIF was converted into N-doped carbon, and the metal ions (Cu²⁺ and Co²⁺) were reduced to metallic Cu and Co [26]. Then, CdS NPs were reduced to metallic Cd and evaporated; free S atoms were released to interact with surrounding N-doped carbon, Co and Cu to form Co-Cu-S and N,S co-doped carbon [27,28]. Meanwhile, the porous N, S dual-doped carbon nanofibers were obtained by the carbonization of CdS@PAN. The Co/Co-Cu-S@SNPCP-CFs shows great flexibility and can be directly used as air electrodes for flexible Zn-air batteries (Figure S4). The crystalline structures of the as-prepared Co/Co-Cu-S@SNPCP-CFs are at first characterized with XRD. As displayed in Figure S5, the XRD pattern of the Co/Co-Cu-S@SNPCP-CFs catalyst is well indexed to the characteristic diffractions of Co (JCPDS No. 15-0806), Co₉S₈ (JCPDS No. 19-0364), Cu_{1.96}S (JCPDS No. 12-0174), and CuCo₂S₄ (JCPDS No. 42-1450). Such metal-sulfide peaks are not observed in the control catalyst of Co/Cu@NPCP-CFs (Figure S6). The energy-dispersive spectrum (EDS) reveals that the Co/Co-Cu-S@SNPCP-CFs contains Co, Cu, S, N, and C elements (Figure S7).

As revealed by SEM images presented in Figure 2(a), the as-prepared Co/Co-Cu-S@SNPCP-CFs are made up of uniform fibers with about several hundred micrometers in length. The result in Figure 2(b) indicates that the carbon

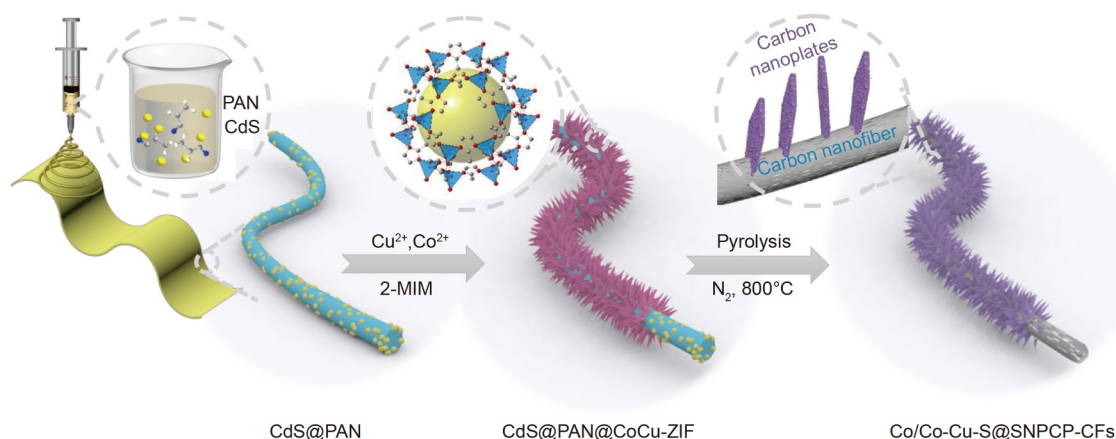


Figure 1 (Color online) Schematic diagram of the Co/Co-Cu-S@SNPCP-CFs synthesis process.

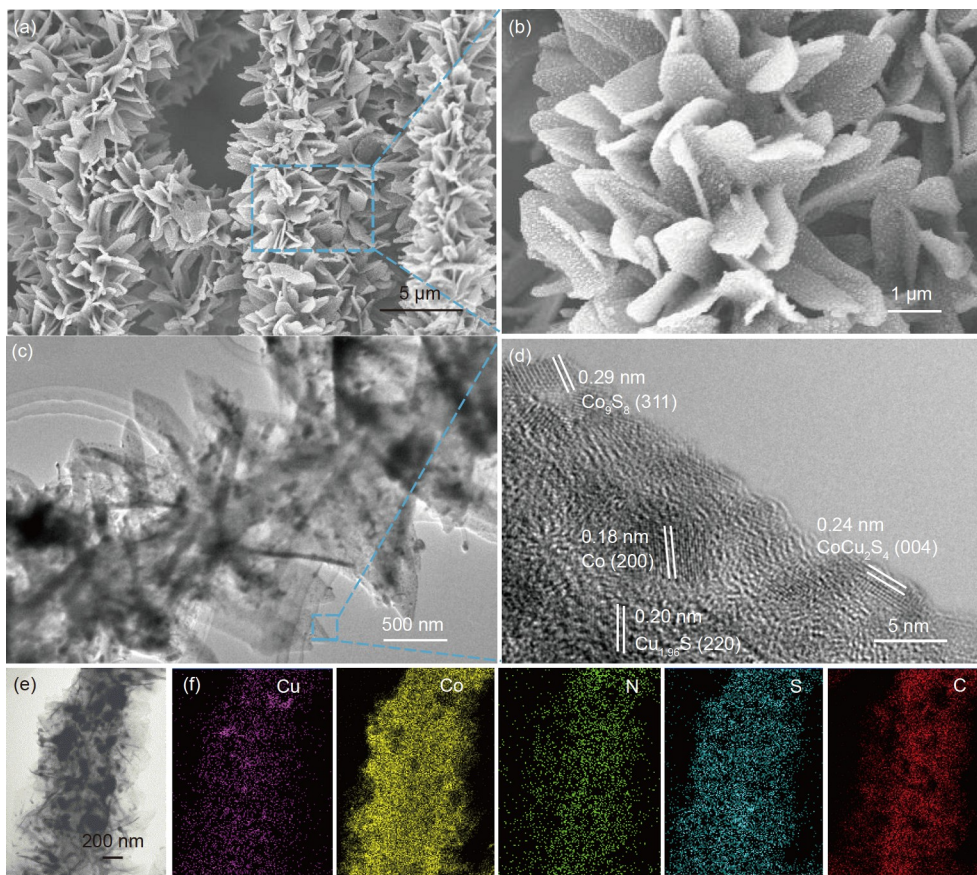


Figure 2 (Color online) (a) and (b) SEM images of the Co/Co-Cu-S@SNPCP-CFs sample; (c) TEM image and (d) HRTEM image of the Co/Co-Cu-S@SNPCP-CFs sample; (e) STEM image and (f) EDS elemental mapping images for Cu, Co, N, S, and C elements of the Co/Co-Cu-S@SNPCP-CFs.

nanofibers are uniformly covered with carbon nanoplates derived from ZIF-L, with the shape well retained. As illustrated in Figure S8, similar structures can also be seen in the control materials of the as-obtained Co/Cu@NPCP-CFs and Co/CoS₂@SNPCP-CFs. The hierarchical porous architecture of the Co/Co-Cu-S@SNPCP-CFs sample is further revealed by TEM image (Figure 2(c)). The interior diameter of the hierarchical structure is about 500 nm, while the exterior layer is mainly constructed with interconnected carbon nanoplates. The HRTEM image of carbon nanoplate shows the lattice fringes with spacings of 0.18, 0.20, and 0.29 nm, which correspond to the plane distances of Co (200), Cu_{1.96}S (220), and Co₉S₈ (311) planes, respectively (Figure 2(d)). Meanwhile, the interplanar spacing of 0.24 nm can be indexed to the (004) planes of CuCo₂S₄. Scanning transmission electron microscopy (STEM) image (Figure 2(e)) and elemental mapping images (Figure 2(f)) show homogeneous distribution of Co, Cu, S, N, and C elements throughout the whole structure.

N₂ adsorption-desorption isotherms and the pore size distribution measurements of the Co/Co-Cu-S@SNPCP-CFs are analyzed. As shown in Figure 3(a), N₂ sorption isotherms show a type-IV isotherm curve with an evident hysteresis loop, indicating the obvious mesoporous structure [29].

Furthermore, the Co/Co-Cu-S@SNPCP-CFs catalyst exhibits the Brunauer-Emmett-Teller (BET) specific surface areas of 332.9 m² g⁻¹, which is greater than those of other control catalysts (Table S1). Furthermore, the Co/Co-Cu-S@SNPCP-CFs possesses the largest pore volumes, revealing the critical involvement of CdS for the formation of porous structure (Figure S9), which is beneficial to the rapid mass transport during the electrochemical process [30,31]. The structural features of carbon in the Co/Co-Cu-S@SNPCP-CFs catalyst are further characterized with the technique of Raman scattering spectroscopy. Two peaks located at 1335 and 1590 cm⁻¹ can be attributed to vibrations relating to defective carbon (D band) and the sp²-graphitic carbon (G band), and their intensity ratio (value of I_D/I_G) provides a significant indicator of the graphitization degree of materials [32,33]. The Co/Co-Cu-S@SNPCP-CFs catalyst has an I_D/I_G value of 0.89 (Figure 3(b)), suggesting a high degree of graphitization of the carbon material, which can facilitate electron transfer during the reaction process for high conductivity [34,35].

To better understand the chemical states of the Co/Co-Cu-S@SNPCP-CFs sample, XPS measurements were performed. The survey spectrum (Figure S10) shows that Co, Cu, S, and N elements are existence on the surface of Co/Co-

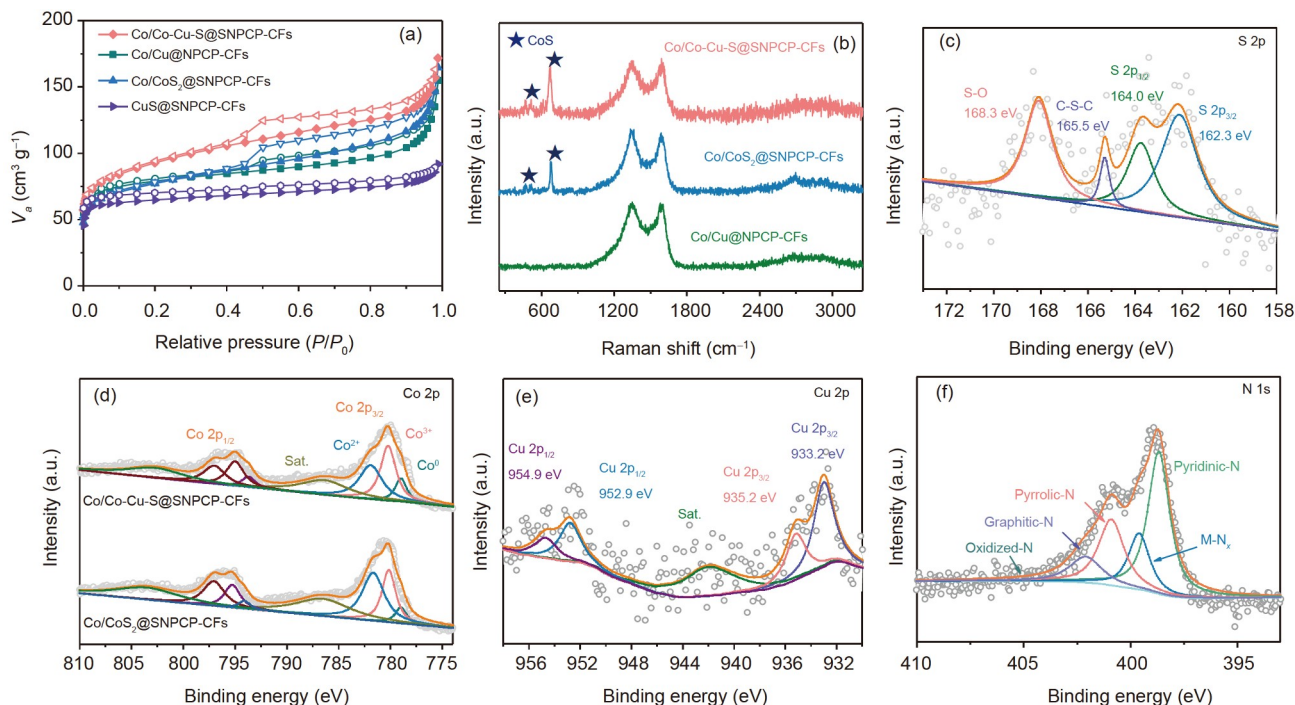


Figure 3 (Color online) (a) N_2 sorption isotherms of the Co/Co-Cu-S@SNPCP-CFs, Co/Cu@NPCP-CFs, Co/CoS₂@SNPCP-CFs, and CuS@SNPCP-CFs samples; (b) Raman spectra of the Co/Co-Cu-S@SNPCP-CFs, Co/CoS₂@SNPCP-CFs, and Co/Cu@NPCP-CFs samples; (c) high-resolution S 2p XPS spectrum of the Co/Co-Cu-S@SNPCP-CFs; (d) high-resolution Co 2p XPS spectra for the Co/Co-Cu-S@SNPCP-CFs and Co/Cu@NPCP-CFs; (e) and (f) Cu 2p and N 1s XPS spectra of the Co/Co-Cu-S@SNPCP-CFs.

Cu-S@SNPCP-CFs catalyst. Quantitative analysis (Table S2) reveals that the corresponding atomic percentages for Co, Cu, S, and N are 4.4%, 0.8%, 1.2%, and 6.9%, respectively. The high-resolution C 1s spectra (Figure S11) for Co/Co-Cu-S@SNPCP-CFs can be fitted into five peaks, corresponding to the C–C (284.8 eV), C–S (285.9 eV), C–N/C–O (286.8 eV), C=O (287.9 eV), and π - π^* (291.6 eV), respectively [36]. Furthermore, the high-resolution S 2p spectra in Figure 3(c) and Figure S12 show the peaks of C–S–C located at 165.5 eV [37,38]. The presence of C–S and C–N bonds demonstrates that the S and N atoms are successfully doped in the skeleton of carbon of Co/Co-Cu-S@SNPCP-CFs product, which can enhance ORR performance by generating an asymmetrical spin/charge density [39]. Additionally, two peaks centered at 162.3 and 164.0 eV are assigned to the S 2p_{3/2} and S 2p_{1/2} states of the S²⁻ species bonded to transition metal atoms (Co/Cu), and the peak at 168.3 eV is contributed to S–O bond [40]. As displayed in Figure 3(d), the high-resolution spectra for Co 2p can be deconvoluted into three spin-orbit doublets corresponded to the Co 2p_{3/2} and Co 2p_{1/2} orbitals of metallic Co (779.0 and 793.7 eV), Co³⁺ (780.2 and 794.9 eV), and Co²⁺ (782.0 and 796.8 eV), while the peaks at 786.4 and 802.7 eV are two shake-up satellites [41–43]. The Cu 2p spectrum (Figure 3(e)) shows two main peaks, corresponding to Cu 2p_{3/2} (933.2 and 935.2 eV) and Cu 2p_{1/2} (952.9 and 954.9 eV), respectively, confirming the co-existence of Cu⁺ and Cu²⁺ in the sample

[44,45]. In comparison, the XPS Cu 2p spectrum of Co/Cu@NPCP-CFs confirms the main presence of metallic Cu and Cu⁺ (Figure S13) [46]. The high-resolution N 1s spectrum (Figure 3(f)) reveals five signals from pyridinic N (398.7 eV), M-N_x (399.6 eV), pyrrolic N (400.9 eV), graphitic N (402.1 eV), and oxidized N (404.8 eV) species [47–49]. It has been reported that the concentration and configuration of N species in carbonaceous catalysts play an important role in ORR process [50]. In particular, pyridinic-N can improve the ORR performance by modulating the electronic on adjacent carbon atoms and supplying active sites [51,52]. The percentage of pyridinic-N in the Co/Co-Cu-S@SNPCP-CFs catalyst increases by ~80% and ~32% compared with those of the Co/CoS₂@SNPCP-CFs and Co/Cu@NPCP-CFs samples (Figure S14 and Table S3), respectively, implying that pyridinic-N species might bond to Cu atoms directly in Co/Co-Cu-S@SNPCP-CFs [53,54].

The bifunctional electrocatalytic performances of the Co/Co-Cu-S@SNPCP-CFs catalyst were tested on a standard three-electrode system. The cyclic voltammograms (CVs) of the Co/Co-Cu-S@SNPCP-CFs catalyst were measured in 0.10 mol L⁻¹ KOH (Figure S15). A clear oxygen reduction peak appears in the O₂-saturated electrolyte comparing with the N₂-saturated electrolyte, which confirms high ORR activity. For comparison, the catalytic activities of the Co/Co-Cu-S@SNPCP-CFs, control samples, and noble-metal catalysts (commercial Pt/C and RuO₂) are evaluated. The linear

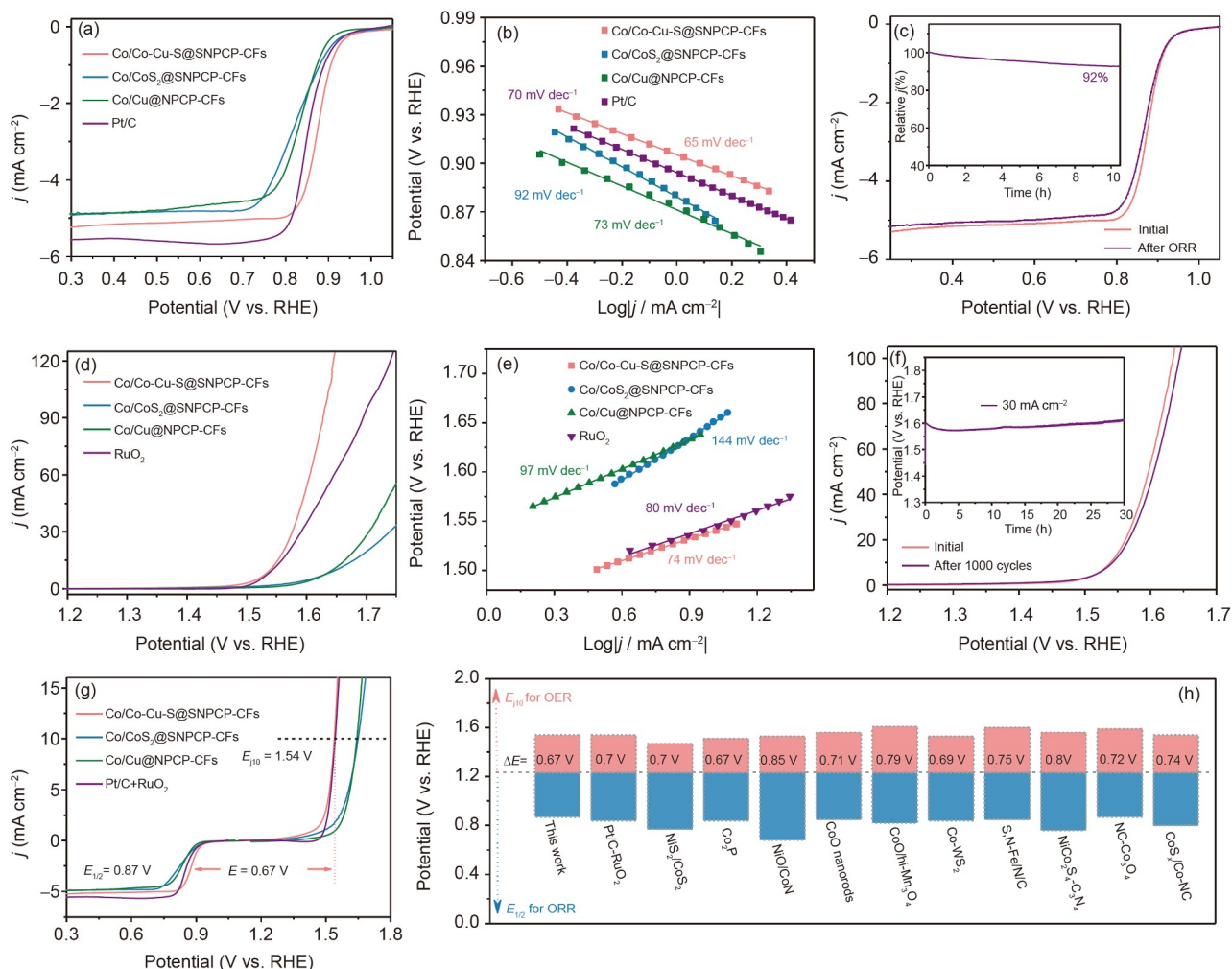


Figure 4 (Color online) (a) ORR polarization curves and (b) Tafel plots of the Co/Co-Cu-S@SNPCP-CFs, Co/CoS₂@SNPCP-CFs, Co/Cu@NPCP-CFs, and Pt/C in 0.10 mol L⁻¹ KOH solution at a rotating speed of 1600 r min⁻¹; (c) chronoamperometric curves and polarization curves before and after ORR process of the Co/Co-Cu-S@SNPCP-CFs catalyst; (d) OER polarization curves and (e) Tafel plots of the as-synthesized catalysts and RuO₂ in 1.0 mol L⁻¹ KOH solution; (f) OER stability test of the Co/Co-Cu-S@SNPCP-CFs catalyst at constant current densities of 30 mA cm⁻² and polarization curves before and after 1000 cycles; (g) the overall LSV curves of OER and ORR activities for all catalysts; (h) comparison of the potential gap (ΔE) values of Co/Co-Cu-S@SNPCP-CFs with recently reported bifunctional electrocatalysts.

sweep voltammetry (LSV) curves exhibit that the Co/Co-Cu-S@SNPCP-CFs sample has the highest onset potential of 0.94 V, an ORR half-wave potential ($E_{1/2}$) of 0.87 V and a diffusion-limited current density of 5.2 mA cm⁻² (Figure 4 (a)), which is much higher than those of Co/Cu@NPCP-CFs ($E_{1/2}$ =0.83 V), Co/CoS₂@SNPCP-CFs ($E_{1/2}$ =0.81 V), Pt/C ($E_{1/2}$ =0.85 V), as well as those recently reported transition metal-based materials (Table S4). The ORR performance of the catalyst with only Cu active sites (denoted as CuS@SNPCP-CFs) is significantly lower (Figure S16), showing that the Co centers are the primary active sites. Figure 4(b) shows the Tafel slope for Co/Co-Cu-S@SNPCP-CFs catalyst is 65 mV dec⁻¹, which is lower than that of Pt/C (70 mV dec⁻¹), implying fast ORR kinetics. The ORR mechanism of the Co/Co-Cu-S@SNPCP-CFs catalyst was further analyzed with rotating disk measurements (Figure S17). The resulting Koutecky-Levich (K-L) plots for Co/Co-

Cu-S@SNPCP-CFs catalyst show good linear relationships at various potentials, suggesting typical first-order reaction kinetics [55]. In addition, the direct four-electron pathway is confirmed by the rotating ring-disk electrode (RRDE) test (Figure S18), which shows that the electron transfer number (n) of Co/Co-Cu-S@SNPCP-CFs is around 4.0, and the H₂O₂ yield remains below 6% at the potential range of 0.3–0.8 V. As shown in Figure 4(c), Co/Co-Cu-S@SNPCP-CFs catalyst exhibits impressive durability with 92% current retention after operating 10 h of constant voltage at 0.6 V. Moreover, almost negligible loss in $E_{1/2}$ and current density is found after the ORR process. The above results demonstrate the better quality of the Co/Co-Cu-S@SNPCP-CFs as ORR electrocatalysts.

Subsequently, the OER performances of various samples were explored in 1.0 mol L⁻¹ KOH electrolyte. The polarization curve (Figure 4(d)) of Co/Co-Cu-S@SNPCP-CFs

displays a low overpotential of 310 mV to reach current density of 10 mA cm^{-2} , which is significantly better than those of Co/Cu@NPCP-CFs, Co/CoS₂@SNPCP-CFs, and comparable to that of RuO₂ catalyst. The outstanding OER kinetics of Co/Co-Cu-S@SNPCP-CFs was depicted by the small Tafel slope of 74 mV dec^{-1} (Figure 4(e)). Furthermore, the electrochemically active surface area (ECSA) tests were measured to determine the intrinsic OER activity based on the double-layer capacitance (C_{dl}) (Figure S19). The C_{dl} of Co/Co-Cu-S@SNPCP-CFs sample (28.7 mF cm^{-2}) is higher than that of Co/CoS₂@SNPCP-CFs (16.1 mF cm^{-2}) and Co/Cu@NPCP-CFs (6.19 mF cm^{-2}), indicating higher activity. The electrochemical impedance spectroscopy (EIS) curves of all samples (Figure S20 and Table S5) were fitted by using a typical equivalent electrical circuit. The charge-transfer resistance (R_{ct}) of the as-obtained Co/Co-Cu-S@SNPCP-CFs catalyst is determined as 0.64Ω , which is obviously lower than that of Co/CoS₂@SNPCP-CFs (5.25Ω) and Co/Cu@NPCP-CFs (1.11Ω). The lowest R_{ct} on the Co/Co-Cu-S@SNPCP-CFs can be attributed to the strong electron coupling between the abundant Co/Co-Cu-S and S,N codoped carbon nanoplates, indicating the enhanced OER and ORR catalytic kinetic and activity. Meanwhile, the Co/Co-Cu-S@SNPCP-CFs catalyst exhibits excellent stability for OER test in alkaline solution (Figure 4(f)). The effects of various Co/Cu ratios on activity are also investigated, which can be easily adjusted by changing the mass of Co(NO₃)₂·6H₂O and Cu(NO₃)₂·3H₂O (Figure S21). Compared with other materials, the catalyst with the Co/Cu ratio of 5:1 had the best ORR and OER performances. In addition, the pyrolysis temperature has a significant impact on electrochemical performance. Thus, Co/Co-Cu-S@SNPCP-CFs prepared at different pyrolysis temperatures from 700 to 900°C were employed to characterize electrocatalytic activity. As shown in Figure S22, the optimum temperature is 800°C, because it exhibits superior performance for both OER and ORR.

The OER and ORR bifunctional activities of all the samples are displayed by the potential gap ($\Delta E = E_{j10} - E_{1/2}$) (Figure 4(g)). Obviously, the reversible oxygen potential of Co/Co-Cu-S@SNPCP-CFs is 0.67 V, lower than that of Pt/C-RuO₂, and also outperforming most reported bifunctional electrocatalysts (Figure 4(h) and Table S4). The outstanding ORR and OER performances of Co/Co-Cu-S@SNPCP-CFs catalyst can be attributed to the following aspects. (1) The different components of Co/Co-Cu-S@SNPCP-CFs materials can introduce more electroactive centers to improve the OER and ORR activities, which significantly promote oxygen catalysis in an alkaline solution. (2) The high accessibility and the diffusion of charges/ions can be possessed by the large specific surface area and the hierarchically porous structure of Co/Co-Cu-S@SNPCP-CFs catalyst [56]. (3) The S,N-codoped carbon nanofibers provide high conductivities

for fast electron transfer and great mechanical properties for structural stability and flexibility [57]. (4) The higher content of pyridinic-N (about 45.0%) can be obtained in the Co/Co-Cu-S@SNPCP-CFs by the introduction of Cu, which can produce positive charges on adjacent sp²-hybridized carbon atoms, thereby accelerating the reaction kinetics of ORR and OER [58]. (5) The synergistic effect between S,N-codoped carbon nanofibers and abundant Co/Co-Cu-S nanoparticles may also contribute to excellent catalytic performance.

To prove the application potential in Zn-air batteries, the bifunctional Co/Co-Cu-S@SNPCP-CFs catalyst was employed as the air electrodes to assemble rechargeable Zn-air battery (Figure 5(a)). The Co/Co-Cu-S@SNPCP-CFs-based battery possesses a higher open-circuit voltage of 1.46 V than that of a Pt/C-based battery (1.43 V) (Figure S23). As exhibited in Figure 5(b), a small voltage drop occurs when the current densities are increased from 2 to 40 mA cm⁻², and discharge resumes reversibly once the current density is reduced, indicating excellent discharge rate performance. Additionally, the smaller voltage gap between the discharge and charge curves of the Co/Co-Cu-S@SNPCP-CFs-based battery also displays its good rechargeable capability (Figure S24), and has a much higher peak power density of 220 mW cm^{-2} at 293 mA cm^{-2} (Figure 5(c)). This peak power performance outperforms both the Pt/C-based battery (96 mW cm^{-2}) and recently reported Zn-air batteries (Table S6). Moreover, the Co/Co-Cu-S@SNPCP-CFs-based battery has a higher specific capacity of $744 \text{ mA h g}_{\text{Zn}}^{-1}$, corresponding to an energy density of 819 W h kg^{-1} at 20 mA cm^{-2} (Figure 5(d) and Figure S25), which is comparable with Pt/C-based battery (Figure S26).

To further evaluate the rechargeability performance, the cycling stability of Zn-air batteries is investigated at constant current density. As seen in Figure S27, the battery assembled with the Pt/C-RuO₂ catalyst fades quickly at the current density of 5 mA cm^{-2} (30 h, 180 cycles), while the Co/Co-Cu-S@SNPCP-CFs-based battery shows exceptionally good stability (800 h and 4800 cycles) at 10 mA cm^{-2} (Figure 5(e)). Such long-lasting cyclability of the Co/Co-Cu-S@SNPCP-CFs catalyst is significantly higher than recently reported materials, as illustrated in Figure 5(f) and Table S6. Figure 5(g) and (h) show that the Co/Co-Cu-S@SNPCP-CFs-based battery remains charge-discharge voltage gap from 0.89 V at the first cycle to 0.97 V at 4800 cycles with a slight voltage drop of 0.08 V. Furthermore, it also exhibits good cycling stability for more than 300 h in the long-term cycling tests at a higher current density of 20 mA cm^{-2} (Figure S28).

To further explore the reasons for the high cycling stability of the Co/Co-Cu-S@SNPCP-CFs catalyst, the cycling tests of Zn-air batteries with control samples are further studied. The battery assembled with the catalyst obtained by the physical mixture of carbon nanoplates and carbon fibers can

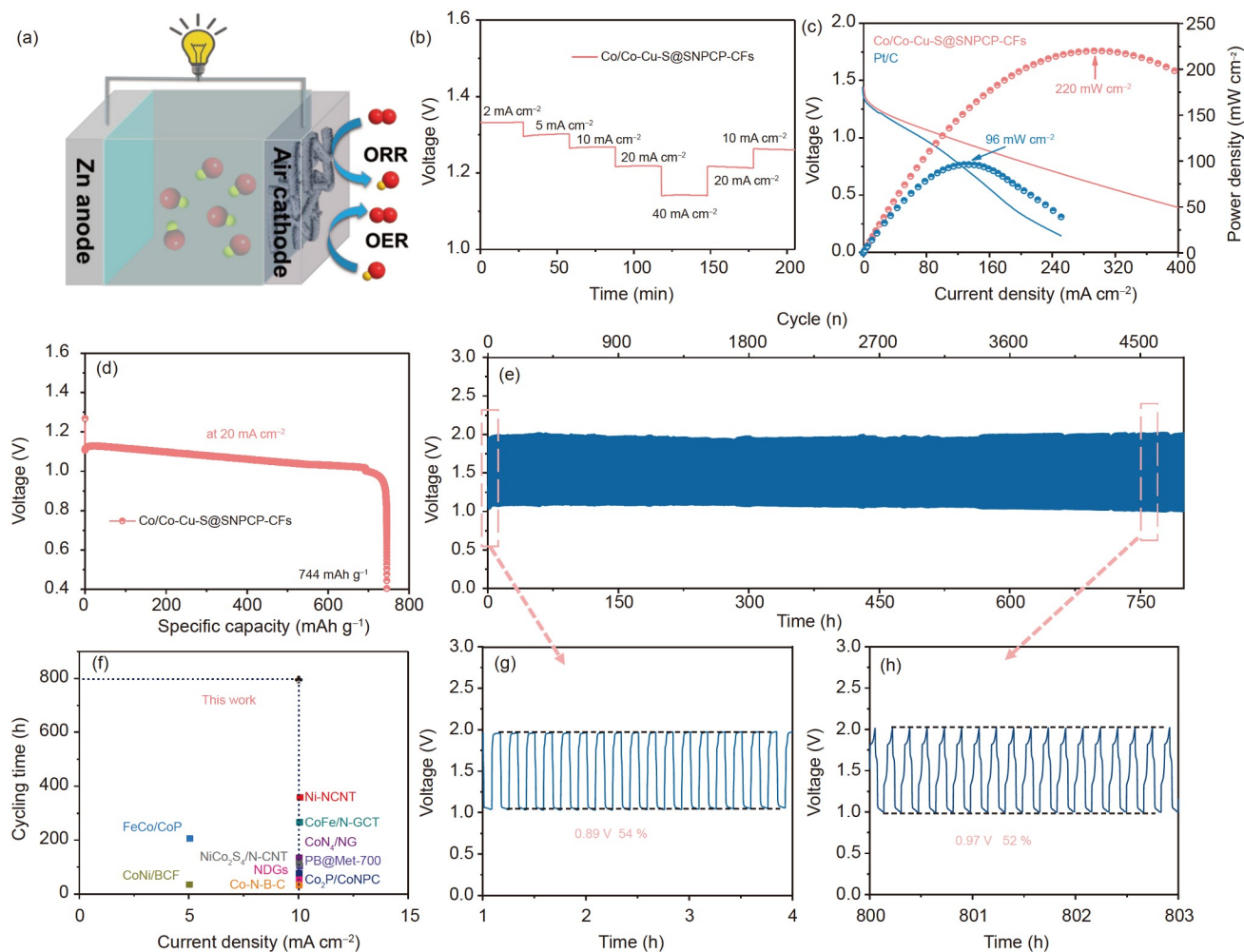


Figure 5 (Color online) (a) Schematic configuration of homemade Zn-air battery; (b) discharge curves of Co/Co-Cu-S@SNPCP-CFs-based Zn-air battery at different current densities; (c) discharge and power density curve of Co/Co-Cu-S@SNPCP-CFs and Pt/C catalysts for Zn-air batteries; (d) discharge specific capacity curves of Co/Co-Cu-S@SNPCP-CFs-based battery at 20 mA cm^{-2} ; (e) cyclic stability of the Co/Co-Cu-S@SNPCP-CFs-based battery at 10 mA cm^{-2} ; (f) cyclability comparison of recently reported catalysts and ours; (g) and (h) voltage variation with cycles of batteries.

only hold about 160 h (960 stable cycles) of charge and discharge (Figure S29), demonstrating the hierarchical mesoporous carbon skeletons can contribute to the stable cycling performance in the charging and discharging cycles [59–61]. The cycling time of the Co/Cu@NPCP-CFs and Co/CoS₂@SNPCP-CFs-based batteries have about 160 and 600 h, respectively (Figures S30 and S31). To further investigate the role of S doping, other metal sulfides such as ZnS and NiS nanoparticles were synthesized according to the previous literature (Figure S32), respectively, which were used as a sulfur source to prepare the final sample (Figure S33) [62,63]. During the pyrolysis process, ZnS nanoparticles can be reduced to metallic Zn by N-doped carbon and metallic Zn can evaporate at 907°C (boiling point of Zn), thereby accelerating the release of free S atoms [64]. However, NiS nanoparticles can only be converted to Ni₃S₂, releasing a small amount of S [65]. It can also be observed that the as-prepared catalyst using ZnS as sulfur sources exhibits excellent cycling stability over 350 h (Figure S34), which are

much higher than the catalyst using NiS as sulfur sources (160 h). As a result, it can be concluded that S doping in this hybrid system improves the stability of Zn-air batteries significantly. As displayed in Figure S35, the air electrode displays good wettability (with a contact angle of 60°) after introducing CdS NPs as S sources, thereby accelerating the diffusion of ions from the electrolyte to the electrode surface [66]. The structural and composition evolution of the Co/Co-Cu-S@SNPCP-CFs catalyst show no discernible change after the cycling test, further demonstrating the robustness of the as-prepared catalyst (Figures S36 and S37).

A flexible Zn-air battery was assembled using a Zn foil anode, Co/Co-Cu-S@SNPCP-CFs film cathode and alkaline gel solid-state electrolyte (Figure 6(a)). The Co/Co-Cu-S@SNPCP-CFs-based flexible batteries show an open-circuit voltage of 1.37 V (Figure 6(b)) and two batteries can power easily light-emitting diodes (LEDs), exhibiting good battery performance. As shown in Figure 6(c), the charge and discharge curves of the Co/Co-Cu-S@SNPCP-CFs-based

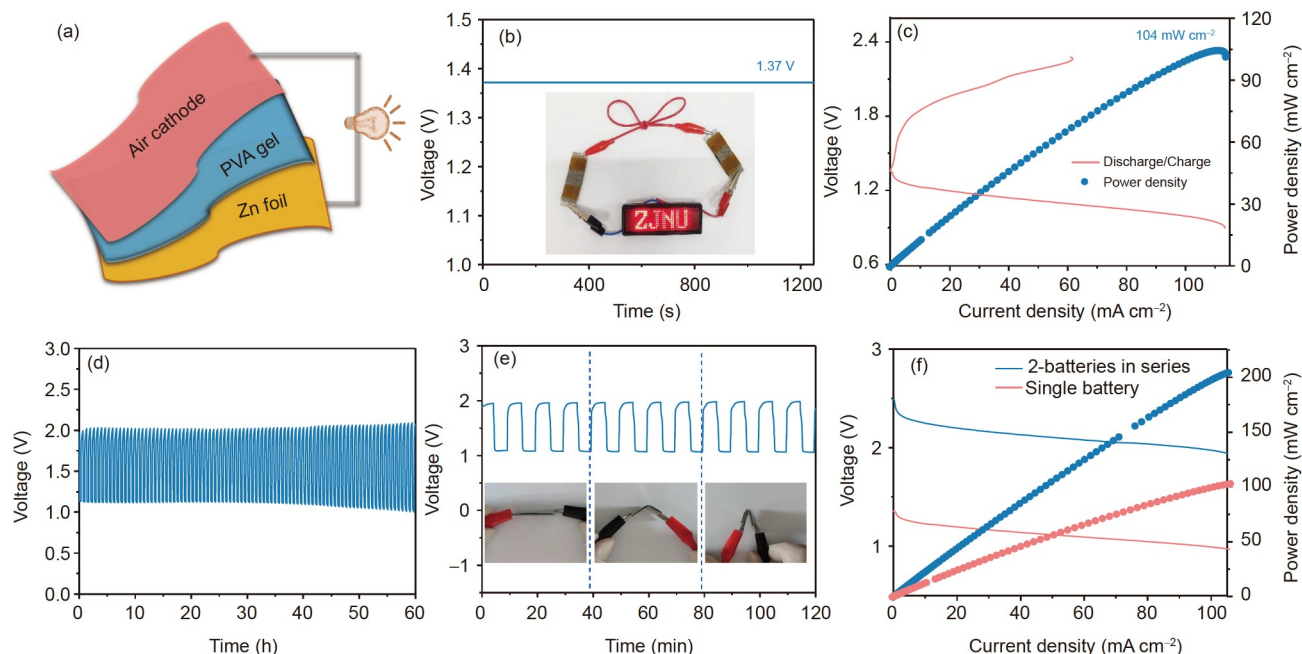


Figure 6 (Color online) (a) Schematic illustration of the flexible solid-state Zn-air battery. (b) Open-circuit voltage measurements for Zn-air battery directly using the Co/Co-Cu-S@SNPCP-CFs as electrode. Inset: a LED screen lighted by two solid-state batteries. (c) Charging/discharging and power density curves of solid-state battery. (d) Long-term cycling performance of solid-state battery at 5 mA cm^{-2} . (e) Galvanostatic charge and discharge curves of solid-state battery under various bending angles. (f) The discharge and power density curves of the two solid-state batteries connected in series and the single.

battery display smaller voltage gap of 0.9 V at 50 mA cm^{-2} , and higher peak power density of 104 mW cm^{-2} . In the long-term cycling test of the Co/Co-Cu-S@SNPCP-CFs-based battery, there is no significant change in charge (2.02 V) and discharge (1.12 V) voltages over 60 h (Figure 6(d)), which is better than previously reported devices (Table S7). The mechanical flexibility test of Co/Co-Cu-S@SNPCP-CFs-based battery is further evaluated by bending condition. After being bent at various angles, the Co/Co-Cu-S@SNPCP-CFs-based battery still work normally, demonstrating that the binder-free electrode structure design can better alleviate the mechanical changes (Figure 6(e)). Moreover, the two in-series batteries can provide twice discharge potential and power density (1.98 V , 198 mW cm^{-2}) than that of the single battery (1.01 V , 99 mW cm^{-2}) at the same current density of 100 mA cm^{-2} (Figure 6(f)), revealing that assembled Zn-air batteries have good application potential as integrated battery systems.

4 Conclusion

In summary, a Co/Co-Cu-S@SNPCP-CFs bifunctional electrocatalyst was rationally designed and used as the free-standing electrodes for long-lifetime rechargeable Zn-air batteries. The hierarchical heteroatom-doped nanostructure has a larger specific surface area and abundant active species, which can endow excellent reaction activity and durability for the oxygen reactions. With the Co/Co-Cu-S@SNPCP-

CFs catalyst as the air cathode, the assembled Zn-air battery can be stably charged and discharged over 800 h with a high peak power density of 220 mW cm^{-2} , outperforming most reported Zn-air batteries. Besides, the flexible solid-state rechargeable Zn-air batteries directly using the Co/Co-Cu-S@SNPCP-CFs catalyst as air electrode display excellent stability over 60 h and shape deformability, indicating a promising application potential in wearable electronics. This study demonstrates the successful synthesis of a high-efficiency bifunctional oxygen electrocatalyst and a novel strategy to develop long-lasting rechargeable metal-air batteries.

This work was supported by the Major Program of Zhejiang Provincial Natural Science Foundation of China (Grant No. LD22B030002), Zhejiang Provincial Ten Thousand Talent Program, and the Independent Designing Scientific Research Project of Zhejiang Normal University (Grant No. 2020ZS03).

Supporting Information

The supporting information is available online at tech.scichina.com and link.springer.com. The supporting materials are published as submitted, without typesetting or editing. The responsibility for scientific accuracy and content remains entirely with the authors.

- 1 Cai X, Lai L, Lin J, et al. Recent advances in air electrodes for Zn-air batteries: Electrocatalysis and structural design. *Mater Horiz*, 2017, 4: 945–976
- 2 Yu X Y, David Lou X W. Mixed metal sulfides for electrochemical energy storage and conversion. *Adv Energy Mater*, 2018, 8: 1701592
- 3 Guo X, Zheng X, Hu X, et al. Electrostatic adsorbing graphene

- quantum dot into nickel-based layered double hydroxides: Electron absorption/donor effects enhanced oxygen electrocatalytic activity. *Nano Energy*, 2021, 84: 105932
- 4 Tan P, Chen B, Xu H, et al. Flexible Zn- and Li-air batteries: Recent advances, challenges, and future perspectives. *Energy Environ Sci*, 2017, 10: 2056–2080
 - 5 Li Y, Lu J. Metal-air batteries: Will they be the future electrochemical energy storage device of choice? *ACS Energy Lett*, 2017, 2: 1370–1377
 - 6 Koper M T M. Thermodynamic theory of multi-electron transfer reactions: Implications for electrocatalysis. *J Electroanal Chem*, 2011, 660: 254–260
 - 7 Wang Y, Zhang G, Ma M, et al. Ultrasmall NiFe layered double hydroxide strongly coupled on atomically dispersed FeCo-NC nanoflowers as efficient bifunctional catalyst for rechargeable Zn-air battery. *Sci China Mater*, 2020, 63: 1182–1195
 - 8 Ji D, Fan L, Tao L, et al. The Kirkendall effect for engineering oxygen vacancy of hollow Co_3O_4 nanoparticles toward high-performance portable zinc-air batteries. *Angew Chem Int Ed*, 2019, 58: 13840–13844
 - 9 Yan L, Xu Z, Hu W, et al. Formation of sandwiched leaf-like CNTs-Co/ZnCo₂O₄@NC-CNTs nanohybrids for high-power-density rechargeable Zn-air batteries. *Nano Energy*, 2021, 82: 105710
 - 10 Liu Q, Wang L, Liu X, et al. N-doped carbon-coated Co_3O_4 nanosheet array/carbon cloth for stable rechargeable Zn-air batteries. *Sci China Mater*, 2019, 62: 624–632
 - 11 Song J, Wei C, Huang Z F, et al. A review on fundamentals for designing oxygen evolution electrocatalysts. *Chem Soc Rev*, 2020, 49: 2196–2214
 - 12 Osgood H, Devaguptapu S V, Xu H, et al. Transition metal (Fe, Co, Ni, and Mn) oxides for oxygen reduction and evolution bifunctional catalysts in alkaline media. *Nano Today*, 2016, 11: 601–625
 - 13 Diao J, Qiu Y, Liu S, et al. Interfacial engineering of $\text{W}_2\text{N}/\text{WC}$ heterostructures derived from solid-state synthesis: A highly efficient trifunctional electrocatalyst for ORR, OER, and HER. *Adv Mater*, 2020, 32: 1905679
 - 14 Wang H, Ye W, Yang Y, et al. Zn-ion hybrid supercapacitors: Achievements, challenges and future perspectives. *Nano Energy*, 2021, 85: 105942
 - 15 Wang W, Kuai L, Cao W, et al. Mass-production of mesoporous MnCo_2O_4 spinels with manganese(IV)- and Cobalt(II)-rich surfaces for superior bifunctional oxygen electrocatalysis. *Angew Chem Int Ed*, 2017, 56: 14977–14981
 - 16 Liu W, Zhang J, Bai Z, et al. Controllable urchin-like NiCo_2S_4 microsphere synergized with sulfur-doped graphene as bifunctional catalyst for superior rechargeable Zn-air battery. *Adv Funct Mater*, 2018, 28: 1706675
 - 17 Chai G L, Qiu K, Qiao M, et al. Active sites engineering leads to exceptional ORR and OER bifunctionality in P,N Co-doped graphene frameworks. *Energy Environ Sci*, 2017, 10: 1186–1195
 - 18 Zheng X, Zhang J, Wang J, et al. Facile synthesis of nickel cobalt selenide hollow nanospheres as efficient bifunctional electrocatalyst for rechargeable Zn-air battery. *Sci China Mater*, 2020, 63: 347–355
 - 19 Zhou T, Shan H, Yu H, et al. Nanopore confinement of electrocatalysts optimizing triple transport for an ultrahigh-power-density zinc-air fuel cell with robust stability. *Adv Mater*, 2020, 32: 2003251
 - 20 Hu X, Luo G, Guo X, et al. Origin of the electrocatalytic oxygen evolution activity of nickel phosphides: *In-situ* electrochemical oxidation and Cr doping to achieve high performance. *Sci Bull*, 2021, 66: 708–719
 - 21 Yang Z, Zhao C, Qu Y, et al. Trifunctional self-supporting cobalt-embedded carbon nanotube films for ORR, OER, and HER triggered by solid diffusion from bulk metal. *Adv Mater*, 2019, 31: 1808043
 - 22 Li Y J, Cui L, Da P F, et al. Multiscale structural engineering of Ni-doped CoO nanosheets for zinc-air batteries with high power density. *Adv Mater*, 2018, 30: 1804653
 - 23 Zhu Y, Zhou W, Shao Z. Perovskite/carbon composites: Applications in oxygen electrocatalysis. *Small*, 2017, 13: 1603793
 - 24 Luo M, Yang Y, Guo S. Precious metal nanocrystals for renewable energy electrocatalysis: Structural design and controlled synthesis. *Dalton Trans*, 2020, 49: 267–273
 - 25 Ji D, Fan L, Li L, et al. Atomically transition metals on self-supported porous carbon flake arrays as binder-free air cathode for wearable zinc-air batteries. *Adv Mater*, 2019, 31: 1808267
 - 26 Kuang M, Wang Q, Han P, et al. Cu, Co-embedded N-enriched mesoporous carbon for efficient oxygen reduction and hydrogen evolution reactions. *Adv Energy Mater*, 2017, 7: 1700193
 - 27 Wang F, Li K, Wang X, et al. Thermal decomposition of CdS nanowires assisted by ZIF-67 to induce the formation of Co_9S_8 -based carbon nanomaterials with high lithium-storage abilities. *ACS Appl Energy Mater*, 2018, 1: 6242–6249
 - 28 Yan L, Wang H, Shen J, et al. Formation of mesoporous Co/CoS/Metal-N-C@S,N-codoped hairy carbon polyhedrons as an efficient trifunctional electrocatalyst for Zn-air batteries and water splitting. *Chem Eng J*, 2021, 403: 126385
 - 29 Wang F, Song S, Li K, et al. A “solid dual-ions-transformation” route to S,N Co-doped carbon nanotubes as highly efficient “metal-free” catalysts for organic reactions. *Adv Mater*, 2016, 28: 10679–10683
 - 30 Tang C, Wang H F, Zhang Q. Multiscale principles to boost reactivity in gas-involving energy electrocatalysis. *Acc Chem Res*, 2018, 51: 881–889
 - 31 Bai J, Meng T, Guo D, et al. Co_9S_8 @ MoS_2 core-shell heterostructures as trifunctional electrocatalysts for overall water splitting and Zn-air batteries. *ACS Appl Mater Interfaces*, 2018, 10: 1678–1689
 - 32 Yu P, Wang L, Sun F, et al. Co nanoislands rooted on Co–N–C nanosheets as efficient oxygen electrocatalyst for Zn-air batteries. *Adv Mater*, 2019, 31: 1901666
 - 33 Kong F, Fan X, Kong A, et al. Covalent phenanthroline framework derived $\text{FeS}@\text{Fe}_3\text{C}$ composite nanoparticles embedding in N-S-codoped carbons as highly efficient trifunctional electrocatalysts. *Adv Funct Mater*, 2018, 28: 1803973
 - 34 Hu E, Yu X Y, Chen F, et al. Graphene layers-wrapped $\text{Fe}/\text{Fe}_3\text{C}_2$ nanoparticles supported on N-doped graphene nanosheets for highly efficient oxygen reduction. *Adv Energy Mater*, 2018, 8: 1702476
 - 35 Lu Z, Wang B, Hu Y, et al. An isolated zinc-cobalt atomic pair for highly active and durable oxygen reduction. *Angew Chem Int Ed*, 2019, 58: 2622–2626
 - 36 Liu L, Zeng G, Chen J, et al. N-doped porous carbon nanosheets as pH-universal ORR electrocatalyst in various fuel cell devices. *Nano Energy*, 2018, 49: 393–402
 - 37 Chen L, Cui L, Wang Z, et al. $\text{Co}_8\text{FeS}_8/\text{N,S}$ -doped carbons derived from Fe-Co/S-bridged polyphthalocyanine: Efficient dual-function air-electrode catalysts for rechargeable Zn-air batteries. *ACS Sustain Chem Eng*, 2020, 8: 13147–13158
 - 38 Kim M J, Park J E, Kim S, et al. Biomass-derived air cathode materials: Pore-controlled S,N-Co-doped carbon for fuel cells and metal-air batteries. *ACS Catal*, 2019, 9: 3389–3398
 - 39 Liang J, Jiao Y, Jaroniec M, et al. Sulfur and nitrogen dual-doped mesoporous graphene electrocatalyst for oxygen reduction with synergistically enhanced performance. *Angew Chem Int Ed*, 2012, 51: 11496–11500
 - 40 Yan L, Ren Y, Zhang X, et al. Electronic modulation of composite electrocatalysts derived from layered NiFeMn triple hydroxide nanosheets for boosted overall water splitting. *Nanoscale*, 2019, 11: 20797–20808
 - 41 Wang H, Yang Y, Li Q, et al. Molecule-assisted modulation of the high-valence Co^{3+} in 3D honeycomb-like Co_xS_y networks for high-performance solid-state asymmetric supercapacitors. *Sci China Mater*, 2021, 64: 840–851
 - 42 Wang S, Wang H, Huang C, et al. Trifunctional electrocatalyst of N-doped graphitic carbon nanosheets encapsulated with CoFe alloy nanocrystals: The key roles of bimetal components and high-content graphitic-N. *Appl Catal B-Environ*, 2021, 298: 120512
 - 43 Chen R, Tan Y, Zhang Z, et al. Hydrazine hydrate induced two-

- dimensional porous Co^{3+} enriched Co_3O_4 nanosheets for enhanced water oxidation catalysis. *ACS Sustain Chem Eng*, 2020, 8: 9813–9821
- 44 Lu W, Yuan Z, Xu C, et al. Construction of mesoporous Cu-doped Co_9S_8 rectangular nanotube arrays for high energy density all-solid-state asymmetric supercapacitors. *J Mater Chem A*, 2019, 7: 5333–5343
- 45 Cheng H, Li M L, Su C Y, et al. CuCo bimetallic oxide quantum dot decorated nitrogen-doped carbon nanotubes: A high-efficiency bifunctional oxygen electrode for Zn-air batteries. *Adv Funct Mater*, 2017, 27: 1701833
- 46 Lu W, Shen J, Zhang P, et al. Construction of CoO/Co-Cu-S hierarchical tubular heterostructures for hybrid supercapacitors. *Angew Chem Int Ed*, 2019, 58: 15441–15447
- 47 Amiin I S, Liu X, Pu Z, et al. From 3D ZIF Nanocrystals to Co- N_x /C nanorod array electrocatalysts for ORR, OER, and Zn-air batteries. *Adv Funct Mater*, 2018, 28: 1704638
- 48 Tang C, Wang B, Wang H F, et al. Defect engineering toward atomic Co- N_x -C in hierarchical graphene for rechargeable flexible solid Zn-air batteries. *Adv Mater*, 2017, 29: 1703185
- 49 Jiang W J, Gu L, Li L, et al. Understanding the high activity of Fe- N_x -C electrocatalysts in oxygen reduction: Fe/ Fe_3C nanoparticles boost the activity of Fe- N_x . *J Am Chem Soc*, 2016, 138: 3570–3578
- 50 Su C, Cheng H, Li W, et al. Atomic modulation of FeCo-nitrogen-carbon bifunctional oxygen electrodes for rechargeable and flexible all-solid-state zinc-air battery. *Adv Energy Mater*, 2017, 7: 1602420
- 51 Masa J, Xia W, Muhler M, et al. On the role of metals in nitrogen-doped carbon electrocatalysts for oxygen reduction. *Angew Chem Int Ed*, 2015, 54: 10102–10120
- 52 Guan C, Sumboja A, Zang W, et al. Decorating Co/ CoN_x nanoparticles in nitrogen-doped carbon nanoarrays for flexible and rechargeable zinc-air batteries. *Energy Storage Mater*, 2019, 16: 243–250
- 53 Wu H, Li H, Zhao X, et al. Highly doped and exposed Cu(i)-N active sites within graphene towards efficient oxygen reduction for zinc-air batteries. *Energy Environ Sci*, 2016, 9: 3736–3745
- 54 Zhang Q, Kumar P, Zhu X, et al. Electronically modified atomic sites within a multicomponent Co/Cu composite for efficient oxygen electroreduction. *Adv Energy Mater*, 2021, 11: 2100303
- 55 Hao Y, Xu Y, Liu W, et al. Co/ CoP embedded in a hairy nitrogen-doped carbon polyhedron as an advanced tri-functional electrocatalyst. *Mater Horiz*, 2018, 5: 108–115
- 56 Xu Y, Deng P, Chen G, et al. 2D nitrogen-doped carbon nanotubes/graphene hybrid as bifunctional oxygen electrocatalyst for long-life rechargeable Zn-air batteries. *Adv Funct Mater*, 2019, 30: 1906081
- 57 Lei Z, Tan Y, Zhang Z, et al. Defects enriched hollow porous Co-N-doped carbons embedded with ultrafine CoFe/Co nanoparticles as bifunctional oxygen electrocatalyst for rechargeable flexible solid zinc-air batteries. *Nano Res*, 2021, 14: 868–878
- 58 Zhang Z, Tan Y, Zeng T, et al. Tuning the dual-active sites of ZIF-67 derived porous nanomaterials for boosting oxygen catalysis and rechargeable Zn-air batteries. *Nano Res*, 2021, 14: 2353–2362
- 59 Zhang Z, Deng Y P, Xing Z, et al. “Ship in a bottle” design of highly efficient bifunctional electrocatalysts for long-lasting rechargeable Zn-air batteries. *ACS Nano*, 2019, 13: 7062–7072
- 60 Tan Y, Zhu W, Zhang Z, et al. Electronic tuning of confined subnanometer cobalt oxide clusters boosting oxygen catalysis and rechargeable Zn-air batteries. *Nano Energy*, 2021, 83: 105813
- 61 Hu X, Luo G, Zhao Q, et al. Ru single atoms on N-doped carbon by spatial confinement and ionic substitution strategies for high-performance Li- O_2 batteries. *J Am Chem Soc*, 2020, 142: 16776–16786
- 62 Jiang N, Tang Q, Sheng M, et al. Nickel sulfides for electrocatalytic hydrogen evolution under alkaline conditions: A case study of crystalline NiS, NiS₂, and Ni₃S₂ nanoparticles. *Catal Sci Technol*, 2016, 6: 1077–1084
- 63 Mahvelati-Shamsabadi T, Goharshadi E K. ZnS nanospheres/reduced graphene oxide photoanode for highly efficient solar water oxidation. *Sol Energy*, 2018, 161: 226–234
- 64 Li Y, Cao R, Li L, et al. Simultaneously integrating single atomic cobalt sites and Co_9S_8 nanoparticles into hollow carbon nanotubes as trifunctional electrocatalysts for Zn-air batteries to drive water splitting. *Small*, 2020, 16: 1906735
- 65 Guo M, Qayum A, Dong S, et al. *In situ* conversion of metal (Ni, Co or Fe) foams into metal sulfide (Ni_3S_2 , Co_9S_8 or FeS) foams with surface grown N-doped carbon nanotube arrays as efficient super-aerophobic electrocatalysts for overall water splitting. *J Mater Chem A*, 2020, 8: 9239–9247
- 66 Jiao Y, Yang C, Wang H, et al. Optimization strategies on the advanced engineering of Co-based nanomaterials for electrochemical oxygen evolution. *J Alloys Compd*, 2021, 890: 161929